Available online at www.sciencedirect.com
ScienceDirect
International Journal of Heat and Fluid Flow 28 (2007) 1112–1124
International Journal of HEAT AND FLUID FLOW
www.elsevier.com/locate/ijhff

Analysis of turbulent flow in channels roughened by two-dimensional ribs and three-dimensional blocks. Part II: Heat transfer

D.N. Ryu [a], D.H. Choi [a,*], V.C. Patel [b]

[a] Department of Mechanical Engineering, Korea Advanced Institute of Science and Technology, Daejeon 305-701, Republic of Korea
[b] IIHR – Hydroscience and Engineering, Department of Mechanical and Industrial Engineering, The University of Iowa, Iowa City, IA 52242, USA

Received 12 May 2005; received in revised form 21 September 2006; accepted 30 November 2006
Available online 7 February 2007

Abstract

The heat-transfer characteristics of a turbulent flow in channels with two-dimensional ribs and three-dimensional blocks are investigated in the context of surface roughness effects. This *Part II* of a two-part paper focuses on heat transfer while *Part I* was devoted to resistance. Reynolds-averaged Navier–Stokes equations, coupled with the k–ω–$\overline{t^2}$–ε_t turbulence model with near-wall treatment for velocity and temperature fields, are solved by a finite-volume method. Calculations are carried out for two-dimensional ribs with square, triangular, semicircular and wavy cross-sections over a range of rib spacing (pitch) and Reynolds numbers. It is found that heat transfer and flow resistance behave in a similar manner, with highest heat transfer occurring when the resistance is maximum. For all cases, the space-averaged temperature profile exhibits a logarithmic region, with a "heat-transfer roughness function" that varies with a constant power of the roughness Reynolds number. The constant power in the formula is found to be slightly larger than that in existing experimental correlations. Analysis of flow with three-dimensional blocks reveals similar characteristics. A log region exists in the space-averaged temperature profile for all cases for which the velocity profile has a log region.

Keywords: Rib; Turbulent heat transfer; RANS equations; k–ω–$\overline{t^2}$–ε_t model; Similarity law

1. Introduction

Regularly distributed two-dimensional ribs or three-dimensional blocks are widely used for heat-transfer augmentation (Webb et al., 1971; Sparrow and Tao, 1983) in heat exchangers, cooling of turbine blades, cooling of electronic devices, etc. The artificial roughness of the surface enhances the heat transfer by breaking the thermal layer and/or invigorating turbulent mixing. However, this is accompanied by undesirable increase in resistance, which was the subject of *Part I* (Ryu et al., in press) of this paper. Heat transfer from artificially roughened surfaces has been extensively studied, but mainly to examine the effects of design variables, such as, channel width-to-height ratio, rib shape, rib height, pitch to height ratio, rib or block orientation, and combinations thereof.

Webb et al. (1971) were perhaps the first to conduct a systematic experimental study on rib-roughened surfaces. They proposed an empirical correlation for the heat-transfer roughness function based on the analogy between heat and momentum transfer. Numerous experimental works on heat-transfer and associated pressure drop for various rib arrangements, angles, and/or shapes are reported in Han et al. (1978), Han (1988), Sparrow and Tao (1983), Liou et al. (1993), Liou and Hwang (1993), Okamoto et al. (1993), and Rau et al. (1998).

The literature on the computational side is also quite extensive. Lee et al. (1988), Acharya et al. (1993), Manceau

* Corresponding author. Tel.: +82 42 869 3018; fax: +82 42 869 3210.
E-mail address: d-h-choi@kaist.ac.kr (D.H. Choi).

0142-727X/$ - see front matter © 2007 Published by Elsevier Inc.
doi:10.1016/j.ijheatfluidflow.2006.11.007

Nomenclature

b, c	length (streamwise) and width (spanwise) of roughness block, Fig. 13
c_p	specific heat at constant pressure
D_e	hydraulic diameter, $2H$
G^+	heat-transfer roughness function, Eq. (7)
H	channel height
h	rib height
h^+	roughness Reynolds number $\left(=\frac{hu_\tau}{\nu}\right)$
k_f	conductivity of fluid
Nu_s	Dittus–Boelter correlation for smooth channel $(=0.023Re_{D_e}^{0.8}Pr^{0.4})$
Pr	Prandtl number $\left(=\frac{\mu c_p}{k_f}\right)$
Pr_t	turbulent Prandtl number $(=\nu_t/\alpha_t)$
q''_w	heat flux from wall to flow $\left(=k_f\frac{dT}{dn}\right)$
Re_δ, Re_{D_e}	Reynolds number $\left(=\frac{\bar{U}\delta}{\nu}$ or $\frac{U_b D_e}{\nu}\right)$
S	substrate thickness $(=0.075H)$
St	Stanton number $(=q''_w/[\rho c_p U_b(T_w - T_{in})])$
$\overline{T_l}$	space-averaged temperature
$\overline{T_b}$	average bulk temperature
$\overline{T_w}$	averaged wall temperature in contact with fluid
$\hat{T}$	normalized temperature $\left(=\frac{T-\bar{T}_{in}}{d\bar{T}_b/dx\cdot D_e}\right)$, Figs. 4, 5 and 14
$\overline{U}$	average velocity between wall and the point of velocity maximum
U_b	bulk velocity
u_τ	space-averaged friction velocity $(=\sqrt{\tau_w/\rho})$
w	rib or block pitch, Figs. 1 and 13
x, y, z	streamwise, normal, and spanwise coordinates, Figs. 1 and 13
$y_{0,T}$	location where T_l is equal to $\overline{T_w}$, virtual origin

Greek symbols

α	thermal diffusivity $\left(=\frac{k_f}{\rho c_p}\right)$
α_t	turbulent thermal diffusivity
δ	distance from wall to the point of velocity maximum
μ	dynamic viscosity
ν, ν_t	kinematic viscosity, eddy viscosity
ρ	density
τ_w	wall shear stress

et al. (2000), Iaccarino et al. (2002), and Tafti (2005) have carried out calculations to examine effects of the aforementioned parameters in addition to the thermal boundary conditions. Although these approaches have adopted sophisticated turbulence closure models that range from two-equation models to large eddy simulations (LES) for the velocity field, a rather simple heat-transfer turbulence model based on the Reynolds analogy, i.e., heat-momentum transport similarity, via a turbulent Prandtl number, is used for the temperature field. More recently, Nagano et al. (2004) performed direct numerical simulations (DNS) to examine the effects of roughness on the statistical quantities in the velocity and thermal fields for channel flows with k- and d-type roughness.

In *Part I* of this paper (Ryu et al., in press), flow resistance in channels with discrete roughness was elucidated in the context of similarity laws of velocity profiles. The primary objective of this second part is to examine the role of similarity laws in the heat-transfer aspect of the problem. A heat-transfer turbulence model that resolves the near-wall region is coupled with the numerical model based on the Reynolds-averaged Navier–Stokes equations that was successfully applied to the rib-roughened surfaces in *Part I*. The existence of a logarithmic layer in the temperature profile is scrutinized and the relevant parameters are identified as was done for the velocity profile. The results provide insights into the validity of the Reynolds analogy that is widely accepted in traditional heat-transfer analyses, and show that the numerical approach may be used to analyze geometries and flow conditions that do not conform to similarity laws.

2. Numerical model and validation

2.1. Governing equations

The equations that govern the steady three-dimensional turbulent incompressible flow are the Reynolds-averaged equations for conservation of mass, momentum, and energy along with the closure relationships for turbulence quantities. In addition to the continuity equation, the Navier–Stokes equations, and the k–ω turbulence model equations already discussed in *Part I*, three additional equations, namely, the internal (thermal) energy equation and two transport equations for the temperature variance $\overline{t^2}$ and its "dissipation rate" ε_t, proposed by Abe et al. (1995), are solved for the heat-transfer characteristics:

Energy:

$$\frac{\partial}{\partial \mathbf{x}}\left[\mathbf{u}T - (\alpha+\alpha_t)\frac{\partial T}{\partial \mathbf{x}}\right] = 0 \tag{1}$$

$$\alpha_t = C_\lambda\left\{\frac{k^2}{\varepsilon}\sqrt{2R} + 3\sqrt{k}\left(\frac{\nu^3}{\varepsilon}\right)^{1/4}\frac{\sqrt{2R}}{Pr}f_d\right\} \times\left\{1-\exp\left(-\frac{n^*}{14}\right)\right\}\left\{1-\exp\left(-\frac{\sqrt{Pr}n^*}{14}\right)\right\},$$

$$C_\lambda = 0.1, \quad R = \tau_t/\tau_u = \left(\frac{\overline{t^2}}{2\varepsilon_t}\right)\Big/\left(\frac{k}{\varepsilon}\right),$$

$$f_d = \exp\left\{-\left(\frac{R_t}{200}\right)^2\right\}, \quad n^* = \frac{(\nu\varepsilon)^{1/4}n}{\nu}$$

where T is temperature, α the thermal diffusivity, α_t the turbulent thermal diffusivity, n the normal distance measured from the wall, R the time scale ratio, and R_t ($=k^2/v\varepsilon$) the turbulent Reynolds number. The equations for the temperature variance $\overline{t^2}$ and its dissipation rate ε_t are solved to calculate the turbulent thermal diffusivity α_t.

Temperature variance:

$$\frac{\partial}{\partial \mathbf{x}}\left[\mathbf{u}\overline{t^2} - \left(\alpha + \frac{\alpha_t}{1.6}\right)\frac{\partial \overline{t^2}}{\partial \mathbf{x}}\right] = 2P_{\overline{t^2}} - 2\varepsilon_t \tag{2}$$

Dissipation rate of $\overline{t^2}/2$:

$$\frac{\partial}{\partial \mathbf{x}}\left[\mathbf{u}\varepsilon_t - \left(\alpha + \frac{\alpha_t}{1.6}\right)\frac{\partial \varepsilon_t}{\partial \mathbf{x}}\right] = C_{P_1} f_{P_1}\frac{\varepsilon_t}{\overline{t^2}}P_{\overline{t^2}} + C_{P_2} f_{P_2}\frac{\varepsilon_t}{k}P_k - C_{D_1} f_{D_1}\frac{\varepsilon_t^2}{\overline{t^2}} - C_{D_2} f_{D_2}\frac{\varepsilon\varepsilon_t}{k} \tag{3}$$

where

$$P_{\overline{t^2}} = \alpha_t \frac{\partial T}{\partial x_j}\frac{\partial T}{\partial x_j}, \quad C_{P_1} = 1.85, \quad C_{P_2} = 0.65,$$
$$f_{P_1} = \{1 - \exp(-n^*)\}^2, \quad f_{P_2} = 1.0, \quad C_{D_1} = 2.0,$$
$$C_{D_2} = 0.9, \quad f_{D_1} = f_{P_1},$$
$$f_{D_2} = \left(\frac{1}{C_{D_2}}\right)(C_{\varepsilon_2} f_2 - 1)\left\{1 - \exp\left(-\frac{n^*}{A_{D_2}}\right)\right\}^2,$$
$$C_{\varepsilon 2} = 1.9, \quad A_{D_2} = 5.5$$

Here, $P_{\overline{t^2}}$ represents the production term in the temperature variance and the various C and f are constants and functions, respectively, in the model transport equations. The details are given in Abe et al. (1995) and are not repeated here. It needs to be noted here that, although the thermal turbulence model described above is capable of predicting the complex thermal field accurately as we shall see later in the paper, the modeled equation (1) becomes nonlinear in T and violates the linearity principle that the energy equation should possess. Readers are encouraged to read Seki et al. (2003) for the details.

2.2. Computational domain and boundary conditions

Since the flow is fully developed, it is periodic in the streamwise direction and, also in the spanwise direction for the three-dimensional case. Then it suffices to consider a limited solution domain, which includes the solid regions of the wall and ribs or blocks as shown in Figs. 1 and 13, and impose periodic conditions at the upstream and downstream boundaries. For a channel with three-dimensional blocks, symmetry conditions are specified at appropriately located spanwise boundaries. The no-slip condition is applied on the upper and lower walls of the channel. The specific dissipation rate, ω is specified at the first grid off the solid surface and given a value $\frac{6v}{(9\Delta n^2/125)}$, where Δn denotes the normal distance from the wall (Wilcox, 1998).

As for the thermal boundary conditions, a uniform heat flux condition is applied on the bottom boundary while the upper wall of the channel is assumed adiabatic. Although the temperature fluctuation at the upstream and downstream boundaries are periodic, the bulk temperature is not periodic in the streamwise direction; the downstream temperature is higher than that of the upstream boundary by a constant $\triangle T$ which is obtained from the total heat flux into the system and the mass flow rate in the channel. The turbulence quantities $\overline{t^2}$ and ε_t need to be specified at the solid–fluid interface and are given the values of zero and $\alpha(\partial\sqrt{\overline{t^2}}/\partial n)^2$, respectively. The dissipation rate at the interface is updated in each iteration and determined as part of the solution.

For a high speed flow, in which the buoyancy force is negligible, the energy equation and associated turbulence transport equations can be decoupled from the fluid-flow equations and solved separately after the flow field has been obtained. The above equations are solved iteratively by a finite-volume method in a non-orthogonal body-fitted colocated grid. Second-order accuracy is preserved by adopting the central differencing scheme throughout. As

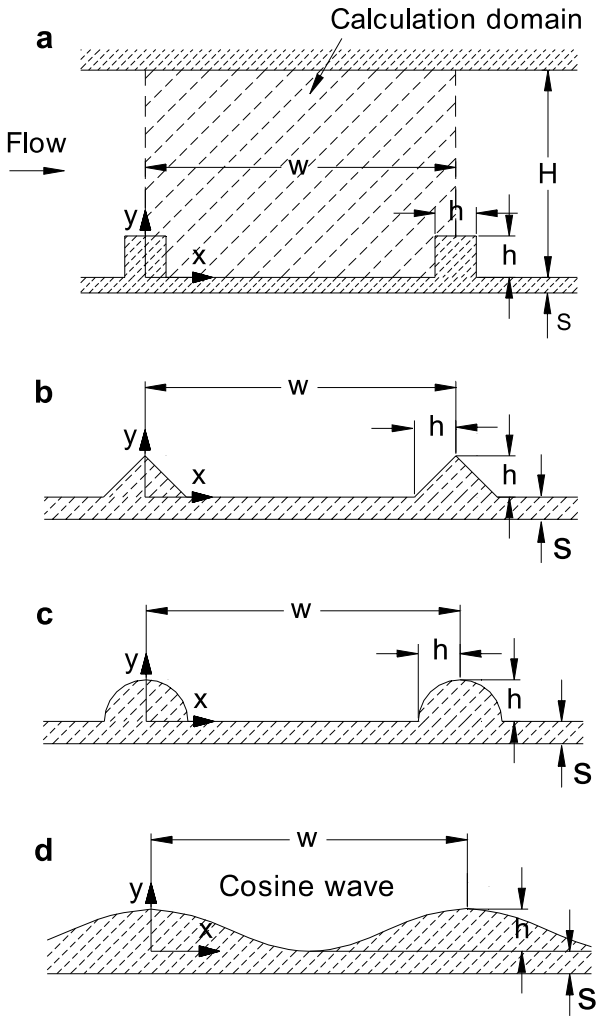

Fig. 1. Schematic of two-dimensional rib-roughened channels and computational domain: (a) square rib, (b) triangular rib, (c) semicircular rib, (d) wavy wall.

mentioned in *Part I*, the QUICK scheme of Hayase et al. (1992) is used to discretize the convective derivatives of the momentum equations. The convergence criteria imposed in the calculation are that the sum of the residuals of mass source is less than 10^{-10} for the velocity field while that of temperature is less than 10^{-6} for the thermal field.

2.3. Validation tests

As in *Part I* of this paper, the scarcity of detailed measured data for the geometric shapes of present interest makes it difficult to validate the model. The model outlined above is first applied to solve the fully developed smooth channel flow with constant heat flux through the wall. The Nusselt number, defined in Eq. (4), is presented in Fig. 2 for a range of Reynolds numbers and is seen to be in excellent agreement with the experimental correlation of Dittus and Boelter (Bejan, 2004). The results of this rather simple flow confirm that the combination of the turbulence models for momentum- and heat-transfer is appropriate.

The code is then validated against two test cases, namely, (a) the backward facing step flow, and (b) the channel flow with uniformly distributed square ribs, for which measured data is available for comparison. These cases have been used by others to validate solution procedures and turbulence models. Since the flow part of the procedure was fully discussed in *Part I* of this paper, it suffices to provide a brief description of the heat-transfer results.

For the backward facing step flow, calculations were performed in a solution domain $-3.8 \leqslant x/h \leqslant 80$ with a 180×80 grid, in which 30 of the 80 grid points are distributed in the expanded region, for a Reynolds number (Re_h), based on the step height and mean inlet velocity, of 28,000, and a Prandtl number (Pr) of 0.71. A constant heat-flux condition is applied at the lower wall of the expanded region and all other solid boundaries are kept adiabatic; the inlet conditions are specified to match the experiments of Vogel and Eaton (1985) while fully developed condition is assumed at the exit boundary.

Fig. 3 shows the isotherms and the streamlines. As already mentioned in *Part I*, the computed reattachment length of $6.78h$ is in excellent agreement with the measured value of $6.68h$. The isotherms in Fig. 3a indicate that the temperature in the recirculation region, especially just downstream of the vertical face of the step, is higher as the fluid is trapped in this region. The local heat transfer along the wall, depicted as the Stanton number, $St = q''_w/[\rho c_p U_b(T_w - T_{in})]$, in Fig. 3b, attains the maximum near the reattachment point and is generally in close agreement with the experiment. Also plotted in the figure is the result obtained by the Reynolds analogy in which the turbulent Prandtl number (Pr_t) is assumed constant everywhere at 0.9 instead of using the $\overline{t^2}$–ε_t model. Interestingly, the two results are not far apart and the need for more sophisticated models does not seem apparent at this level of detail in this particular flow. It is of interest, however, to compare the turbulent Prandtl number implied by the

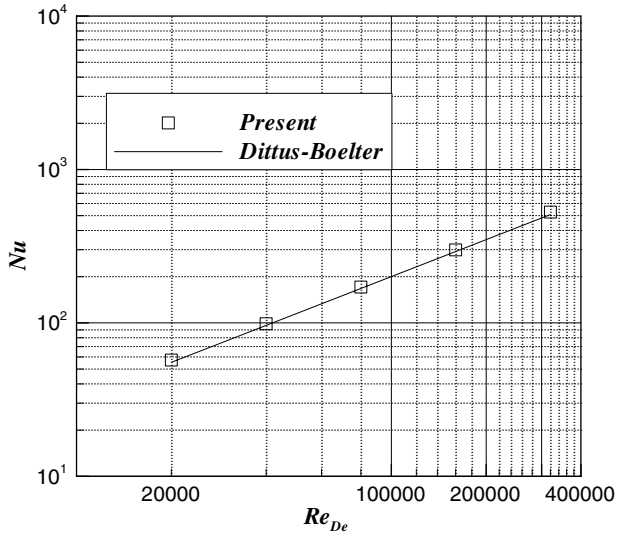

Fig. 2. Nusselt number vs. Re_{D_e} for smooth channel flow with uniform heat flux.

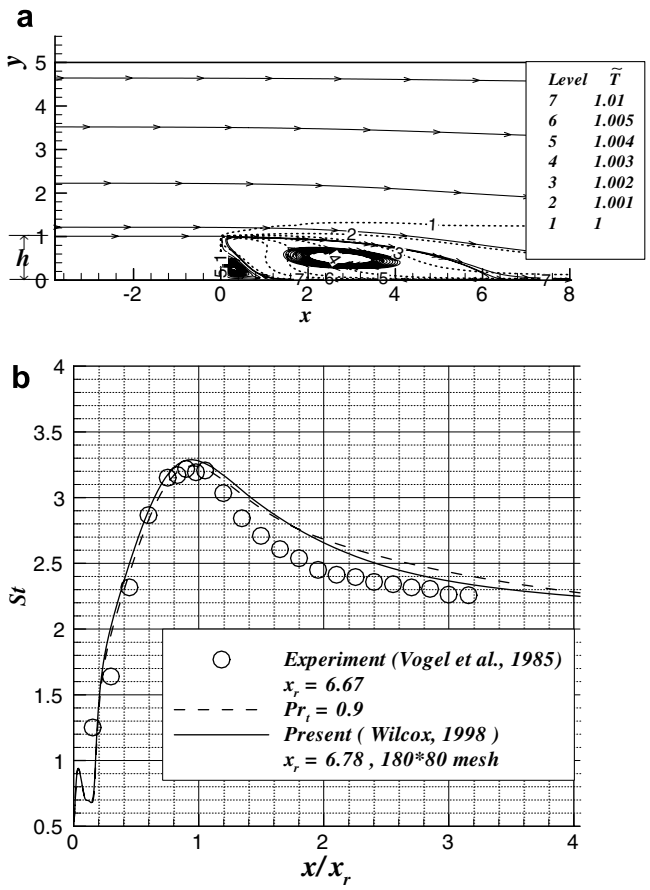

Fig. 3. Backward facing step flow for $Re_h = 28{,}000$ and $\delta_b/h = 1.1$ at $x/h = -3.81$: (a) streamlines and temperature ($\tilde{T} = T/T_{in}$) contours, (b) St distribution along the channel.

turbulence model with the constant value. This is done in the next test case.

The last validation test case is the square-ribbed channel flow with $w/h = 7.2$ at $Re_{D_e} = 12,600$, where w is the rib spacing, h the rib height, and D_e is the hydraulic diameter of the channel. The rib and the channel wall (or substrate) are made of the same material (aluminum), and the wall thickness is set at $0.0375D_e$ to recreate the experimental setup of Liou et al. (1993). After testing a few non-uniformly distributed grids (with 80×80, 100×100, and, 120×120 points), the 100×100 grid, with 20 points placed in the substrate, was chosen to fit the computational domain shown in Fig. 1a. Since the geometry is typical of the present study, this particular grid is used studying all subsequent calculations. The streamlines, isotherms and the local Nusselt number, which is defined as

$$Nu = \frac{-\frac{dT}{dn} \cdot D_e}{(T_w - T_b)} \tag{4}$$

where T_b is the local bulk temperature,

$$T_b = \frac{\int_0^H T|u|\,dy}{\int_0^H |u|\,dy} \tag{5}$$

are presented and compared with the measured data of Liou et al. (1993) in Fig. 4.

It is found that the temperature is generally higher in the recirculation region and attains the maximum near the back-face corner of the rib. Consequently, the substrate temperature is higher under this area as seen in Fig. 4a. The fluid temperature is locally so high that heat flows from the fluid to the rib through certain portions of the vertical face (Fig. 4b). A similar result was reported by Manceau et al. (2000). The local Nusselt number distribution compared in Fig. 4b shows some discrepancy between the experiment and present calculations, especially over the rib surface. It is not clear how Nu was evaluated by Liou et al. As the local heat flux is difficult to measure in experiments, the calculation is repeated without the substrate, with the heat-flux through the base of the rib distributed equally to the three rib faces, as was done by Manceau et al. Interestingly, the Nu distribution obtained in this manner agrees better with the experiment than the results with the finite channel-wall thickness. The results of Manceau et al., also plotted in Fig. 4b compare less favorably with the measured data, presumably due to a simple heat-transfer turbulence model in which a curve-fit formula is used to obtain the turbulent Prandtl number and hence the turbulent thermal diffusivity. Because of uncertainties in the experiment, no further attempt is made to resolve the discrepancies. Unlike in the case of backward facing step flow, the constant turbulent Prandtl-number approach performs very poorly as the results deviate wildly from those of the $\overline{t^2}$–ε_t model or the experimental data, as can be seen in the figure. This led us to more closely examine the behavior of the turbulent Prandtl number predicted by the model equations. The Pr_t distribution across the

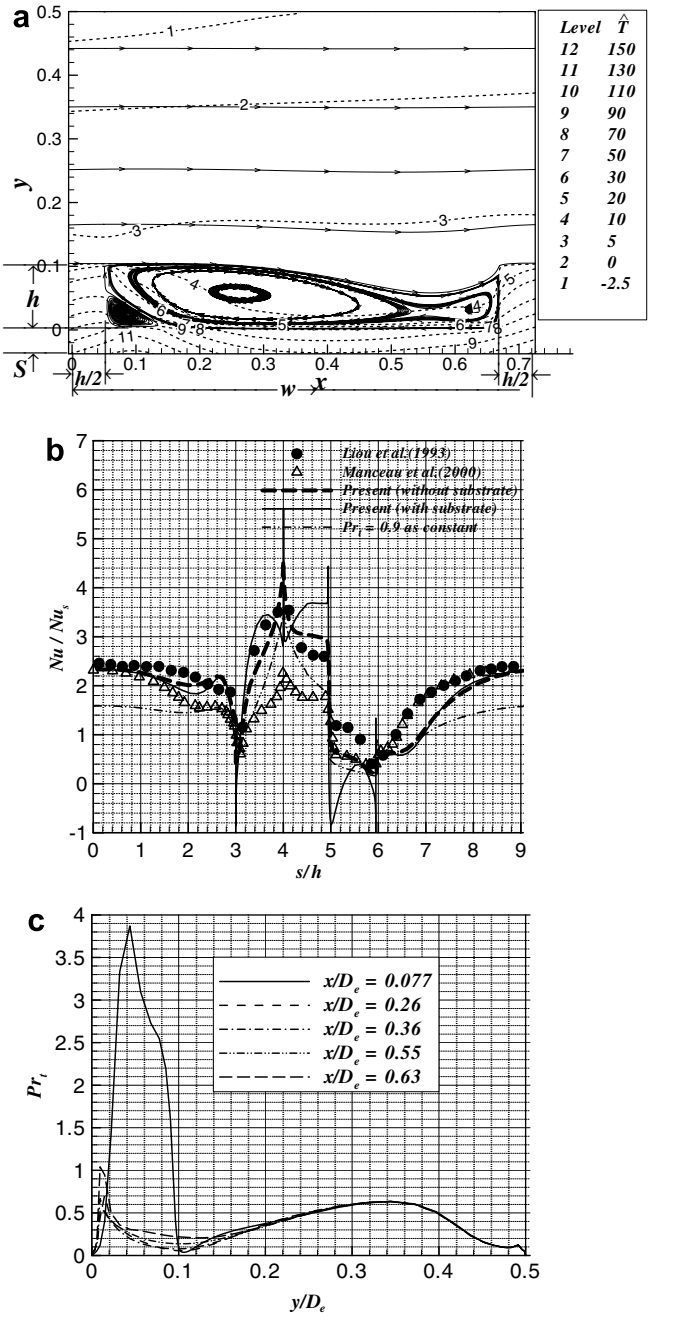

Fig. 4. Periodic square rib distributed channel flow for $w/h = 0.72$, $h/D_e = 0.1$ at $Re_{D_e} = 12,600$: (a) streamlines and temperature distribution, (b) Nusselt number distribution along the channel/rib surface (s is measured from $3h$ upstream of the front rib face), (c) Pr_t distributions across the channel at various streamwise stations.

channel at various cross-sections presented in Fig. 4c shows that Pr_t varies appreciably from very large values just behind the rib to small values in the vicinity of the dividing streamline that emanates from the top of the rib surface. It is also noted that Pr_t does not become constant even in the region far from the rib. This may be attributed to the fact that the flow Reynolds number is rather low. We return to this point later in the paper. All of these results imply that the velocity–temperature analogy is not valid at the local

level and the constant turbulent Prandtl-number assumption is a gross over simplification.

3. Results and discussion

3.1. Heat transfer over two-dimensional ribs

The various cases examined for flow resistance in *Part I* of this paper, namely, spanwise ribs of three shapes (square, triangular, and semicircular) and a wavy wall with the same height as the ribs, are considered for the heat transfer study. With air as the fluid ($Pr = 0.71$), calculations are carried out for a range of Reynolds numbers and rib spacing or pitch (w). The rib height and the substrate thickness are held constant at $h/D_e = 0.1$ and $S/D_e = 0.0375$, respectively. The rib and the substrate are made of aluminum as in the second test case discussed in the previous section. The thermal conductivity ratio of aluminum to air is 9.01. It is appropriate to mention here that calculations can be carried out just as easily without a substrate but they are not pursued as they represent an ideal situation that cannot be reproduced in reality.

Fig. 5 presents the streamlines and isotherms for square and triangular ribs for $Re_{D_e} = 20,000$ and $w/h = 10$. The temperature is higher, in general, under the rib as the solid region is thicker, and also in the recirculation zone. For ribs of square and semicircular shape, a secondary recirculation zone is formed near the rib-wall juncture behind the rib and the substrate temperature under this region becomes very high. The fluid in the secondary recirculation zone is heated, sometimes hotter than the rib itself, and the heat flows from the air to the solid, as was observed in the second test case above. This phenomenon is clearly depicted in Fig. 6, which shows the heat flux and temperature distributions along the channel surface for all rib shapes. Here the temperature difference between the solid surface and the local bulk temperature defined in Eq. (5) is plotted. It is seen that the temperature is lowest on the windward face of the rib and highest on the leeward face, while the heat flux is highest on the front face and lowest on the back face.

The average Nusselt number Nu_{av} for various rib shapes for a range of pitch ratio (w/h) and Reynolds number, $Re_\delta (= \overline{U}\delta/\nu)$, is shown in Fig. 7. As in *Part I*, δ is the distance measured from the channel wall to the point where the space-averaged velocity reaches the maximum and $\overline{U}$ is the average velocity obtained by integration of the velocity profile from the lower wall to δ. The average Nusselt number is defined as:

$$Nu_{av} = \frac{\overline{q''_w} \cdot D_e}{k_f(\overline{T_w} - \overline{T_b})} \tag{6}$$

where the average heat flux $\overline{q''_w}$ is equal to the heat flux specified as the boundary condition, and $\overline{T_w}$ and $\overline{T_b}$ denote the

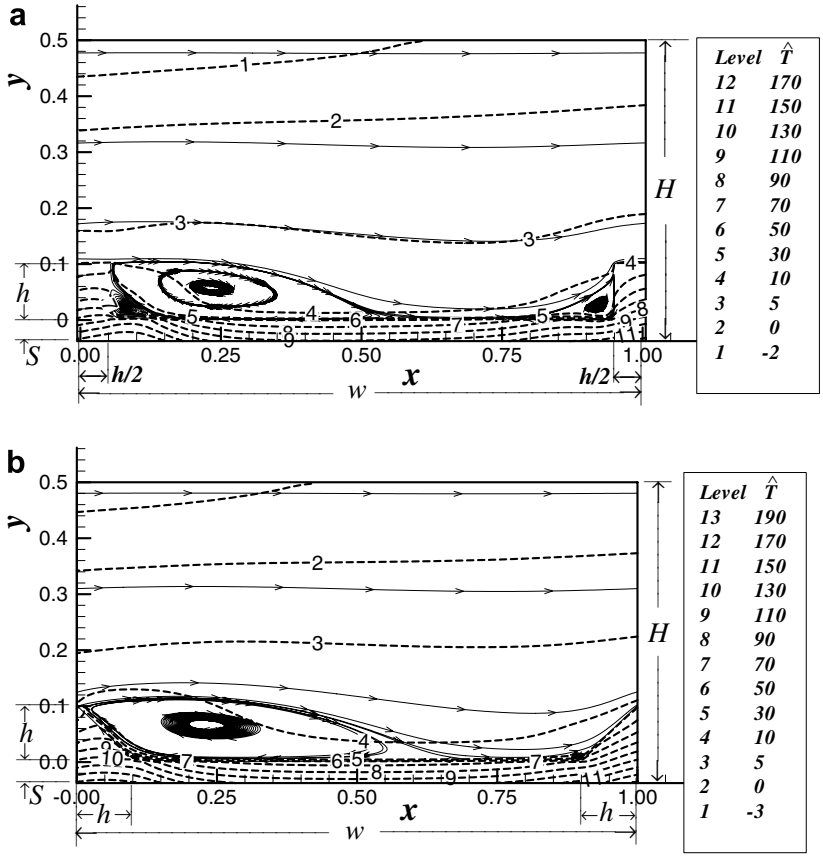

Fig. 5. Streamlines and temperature field for $Re_{D_e} = 20,000$ and $w/h = 10$: (a) square rib, (b) triangular rib.

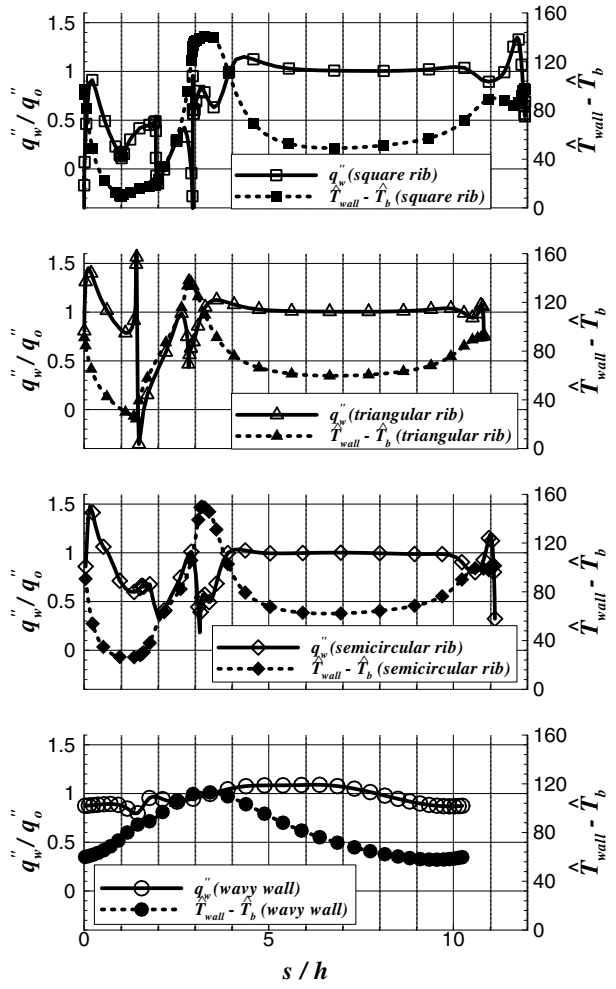

Fig. 6. Heat flux and wall temperature along the channel surface for various shapes for $w/h = 10$, $h/D_e = 0.1$ and $Re_{D_e} = 20,000$ (s is measured from the front rib-wall juncture or the peak of the wavy wall; q''_0 denotes the heat flux applied at the boundary).

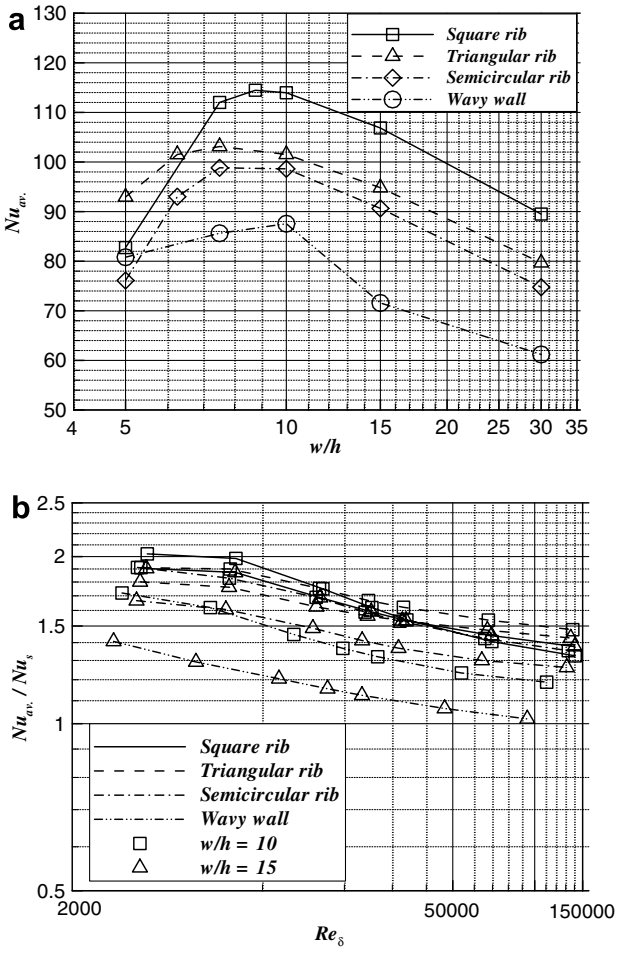

Fig. 7. Average Nusselt number for various shapes for $h/D_e = 0.1$: (a) vs. pitch at $Re_{D_e} = 20,000$, (b) vs. Reynolds number.

average surface temperature and bulk temperature of the air, respectively. For all rib shapes, the Nusselt number initially increases with increasing pitch, reaches a maximum, and gradually decreases toward the smooth-wall limit. In general, the heat transfer is enhanced most by the square rib, and decreases as the shape changes to triangular, to semicircular, and to a wavy wall. In fact, this behavior parallels that of flow resistance reported in *Part I*. This confirms that, in general, heat-transfer enhancement is achieved at the expense of increased resistance. The fact that there exists an optimum value of rib spacing for maximum heat transfer and that the heat-transfer rate does not increase with the rib-surface area suggests that the primary cause for the enhancement is the strong turbulent motion induced by the rib. The behavior at lower pitch ratio in the case of square ribs, which deviates from the general trend, is because the square ribs exhibit "d-type" roughness behavior as the rib spacing becomes small: a single eddy is trapped between the adjacent ribs and hinders the heat transfer.

The Nusselt number for various rib shapes is plotted against the Reynolds number based on δ, Re_δ, in Fig. 7b for pitch ratios of 10 and 15. The Dittus–Boelter empirical formula for a smooth surface, Nu_s, is used for comparison. Calculations have been made for the range of Re_{D_e} from 10,000 to 320,000 to complete the figure. The Nusselt number monotonically decreases towards the smooth surface limit of unity as Re_δ increases. The effectiveness of distributed ribs in heat-transfer enhancement is more noticeable in the low Reynolds-number region than at higher Reynolds numbers. The slope for the square ribs appears to be steeper than those for other rib shapes.

As in the velocity profile for rough surfaces, the temperature distribution is also expected to exhibit similarity law when plotted in wall variables (Kays and Crawford, 1993):

$$T^+ = \frac{Pr_t}{\kappa} \ln\left(\frac{y - y_{0,T}}{h}\right) + G^+ \tag{7}$$

with the dimensionless temperature T^+ defined as

$$T^+ = (\overline{T_w} - T_1)\rho c_p u_\tau / \overline{q''_w} \tag{8}$$

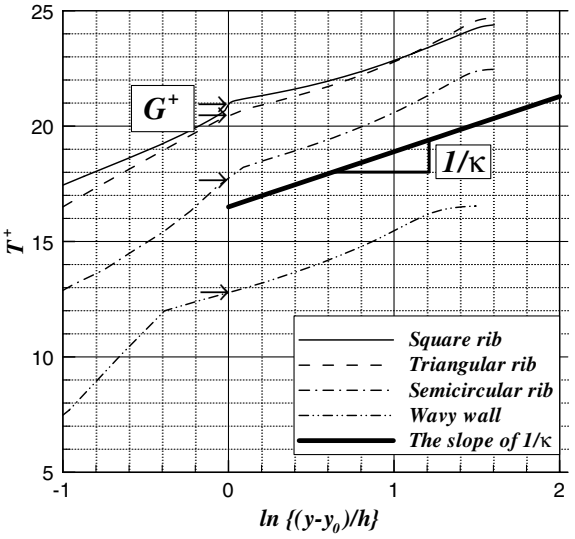

Fig. 8. Space-averaged temperature profiles in wall coordinates for various rib shapes for $w/h = 10$, $h/D_e = 0.1$ and $Re_{D_e} = 20,000$.

where T_l is the space-averaged temperature at y, $\overline{T}_w$ is the averaged wall temperature at the solid–fluid interface, and $\overline{q''_w}$ is the averaged heat flux across the interface.

Fig. 8 shows the space-averaged temperature profiles for various ribs in the wall coordinates. When necessary, a four-point bilinear interpolation is used to obtain the temperatures at desired locations from those in the generalized computational grids. The average temperature may be higher above the wall than at the wall because of the higher temperature in the recirculation zone. The virtual origin is thus identified as the point at which the space-averaged temperature equals the mean wall temperature. It is important to note here that the virtual origins for velocity and temperature are not the same. The temperature profiles for all cases clearly exhibit a significant logarithmic region which, in most cases, starts above the top of the rib. The slope varies from one case to another but is, in general, relatively close to that of the velocity profile, i.e., $1/\kappa$, implying that Pr_t in the coefficient of Eq. (7) is close to 1, which is in line with the experimental observation for smooth surfaces (Kays and Crawford, 1993) or that used in Dipprey and Sabersky (1963) for sand grain roughness. Some caution is in order, however. As noted above, the log profile with the slope near $1/\kappa$ is valid only when the virtual origin, and not the physical boundary, is used as the datum. The existence of the log region together with its constant slope is a most interesting and significant result because it implies that similarity exists in the space-averaged temperature field just as in the velocity profiles discussed in *Part I*. The turbulent Prandtl number distribution is further investigated for a range of Reynolds numbers and is shown for two Reynolds numbers in Fig. 9. The profiles for $Re_{D_e} = 20,000$ at various cross-sections in Fig. 9a show that Pr_t varies substantially across the channel and from upstream to downstream. It becomes quite large in the recirculation region behind the rib and small along the

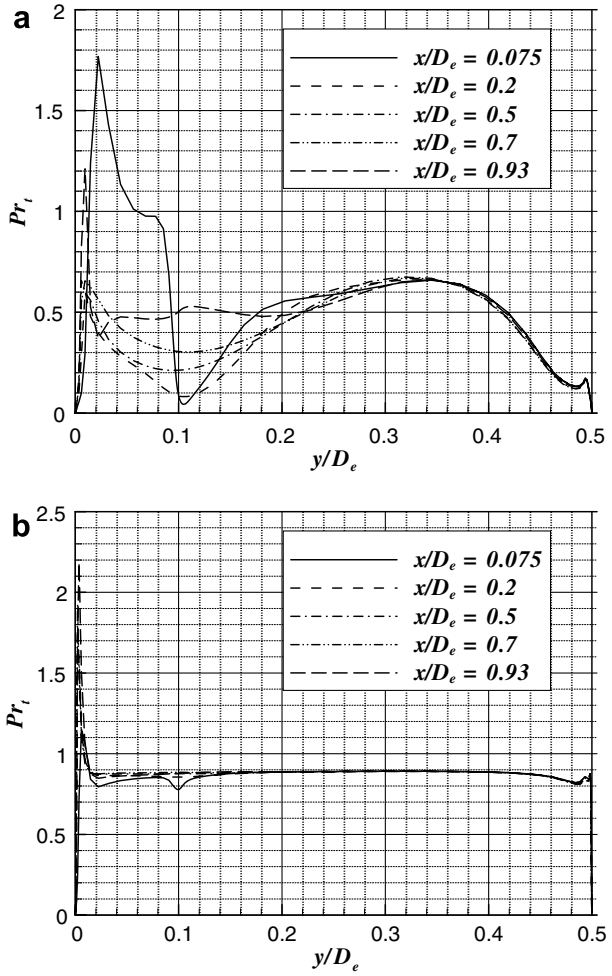

Fig. 9. Turbulent Prandtl number distributions at various streamwise cross-sections for the square rib with $w/h = 10$, $h/D_e = 0.1$: (a) $Re_{D_e} = 20,000$, (b) $Re_{D_e} = 160,000$.

dividing streamline near $y/D_e \approx 0.1$. It increases gradually toward the center of the channel but does not remain constant for any significant portion of the channel. However, for $Re_{D_e} = 160,000$, Pr_t remains almost constant – this value approaches unity as the Reynolds number further increases – everywhere except very near the wall. This suggests that the complete Reynolds analogy ($Pr_t = 1$) may exist for rib-roughened surfaces at very high Reynolds numbers.

It is appropriate to elaborate here on the asymptotic behavior of $Pr_t(=\nu_t/\alpha_t)$ near the surface. For attached flow on smooth surfaces, the experimental Pr_t is known to increase as the wall is approached while some DNS results show it to remain near unity (Kays, 1994). Kasagi et al. (1989) showed, in their numerical study, that Pr_t approaches to either a finite value or zero at the wall depending on the thermal wall boundary condition. Although the present result of decreasing Pr_t is in line with their findings for the constant heat-flux wall, the comparison is of no significance as the k–ω model predicts an order smaller Reynolds stress ($\sim y^4$) than the correct value ($\sim y^3$)

close to the wall. Despite the flaw in the limiting behavior, the model's ability to predict the properties of interest in the turbulent boundary layer was shown to be not affected much because the discrepancy is confined to a small region close to the wall and ν_t is negligibly small there (Wilcox, 1998). This is also confirmed in the present study as seen in Fig. 2.

Fig. 10 shows the virtual origin for various rib shapes. Other than the wavy wall, the virtual origin $y_{o,T}$ is much smaller than that for the velocity field reported in *Part I*. It decreases monotonically to zero with increasing w/h for all rib shapes. When plotted against the dimensionless roughness $h^+(=hu_\tau/\nu)$ for a given w/h, however, it eventually starts to increase after an initial decrease. This is quite different from the virtual origin of the velocity field, and is because of the fact that the increased cooling lowers the average wall temperature while the fluid temperature in the recirculation region is less affected by an increase of h^+.

The heat-transfer roughness function G^+ of Eq. (7) can be deduced from the computed temperature field and is presented in Fig. 11. For all rib shapes, G^+ is seen to decrease with the pitch ratio and is proportional to h^+ in

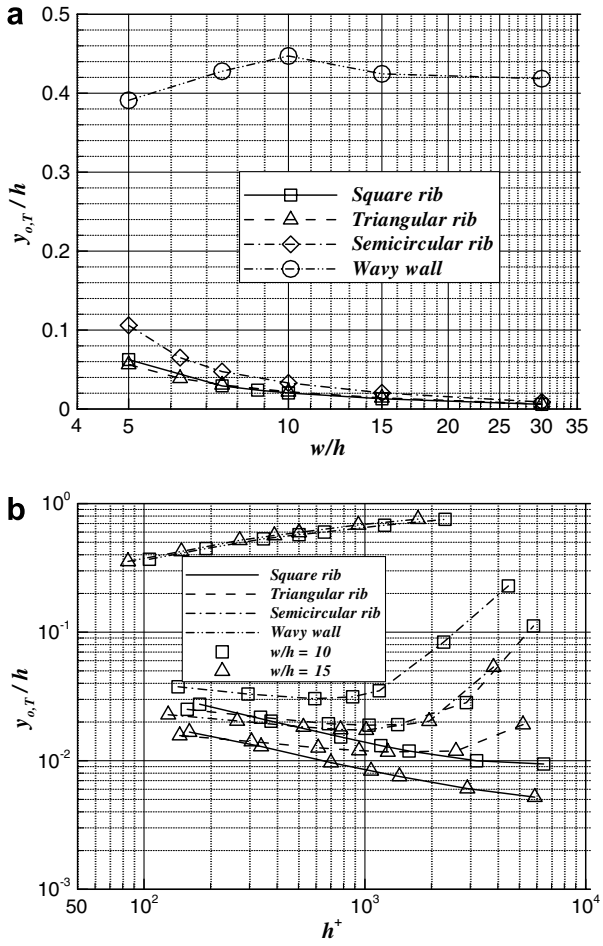

Fig. 10. Location of virtual origin for various rib shapes for $h/D_e = 0.1$: (a) vs. pitch at $Re_{D_e} = 20,000$, (b) vs. h^+.

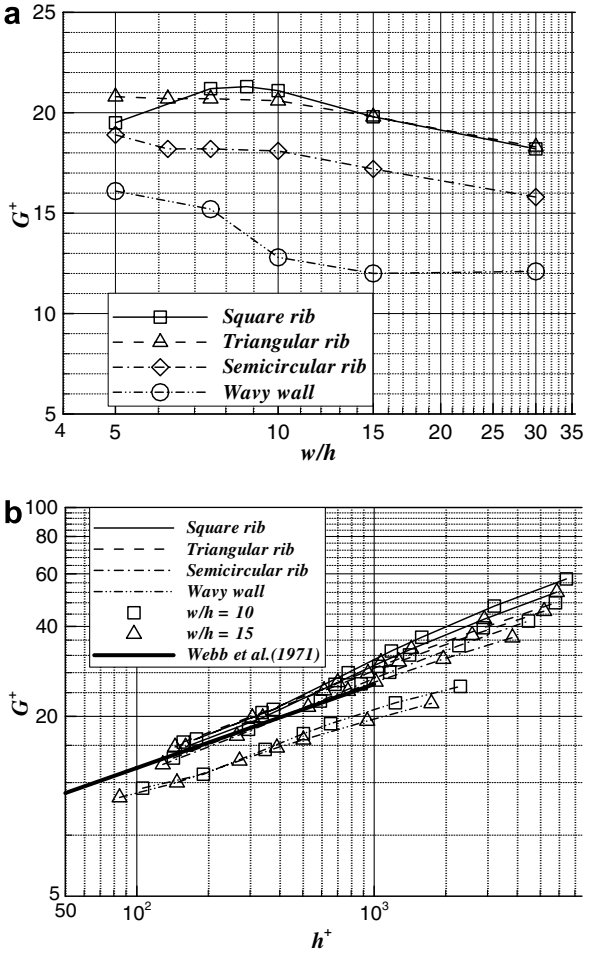

Fig. 11. Heat transfer roughness function for $h/D_e = 0.1$: (a) vs. pitch at $Re_{D_e} = 20,000$, (b) vs. h^+.

log–log scale. All curves are packed together except those for the wavy wall, which are considerably lower than the others. The empirical correlation of Webb et al. (1971), which is based on measurements up to $h^+ = 1000$ for ribs of rectangular shape, is also plotted in Fig. 11b for comparison:

$$G^+ = 4.5(h^+)^{0.28}(Pr)^{0.57} \tag{9}$$

The two are in general agreement, but the slope of the present numerical results is steeper.

To further characterize rib-roughened surfaces, a series of calculations is carried out for square ribs of various sizes (h/D_e) and pitch ratios (w/h). The results are summarized in Fig. 12. The Nusselt number relative to that for the smooth surface is presented in Fig. 12a. As was observed earlier in Fig. 7b, the Nusselt number gradually decreases and approaches the smooth-surface limit as Re_δ increases. For the same pitch ratio, the Nusselt number is generally larger for a larger rib size as the flow is disturbed more. There appears to be a point where the relative Nusselt number attains a maximum value and then decreases as Re_δ further decreases. This is more pronounced as the rib size and pitch ratio become smaller. The heat-transfer roughness function

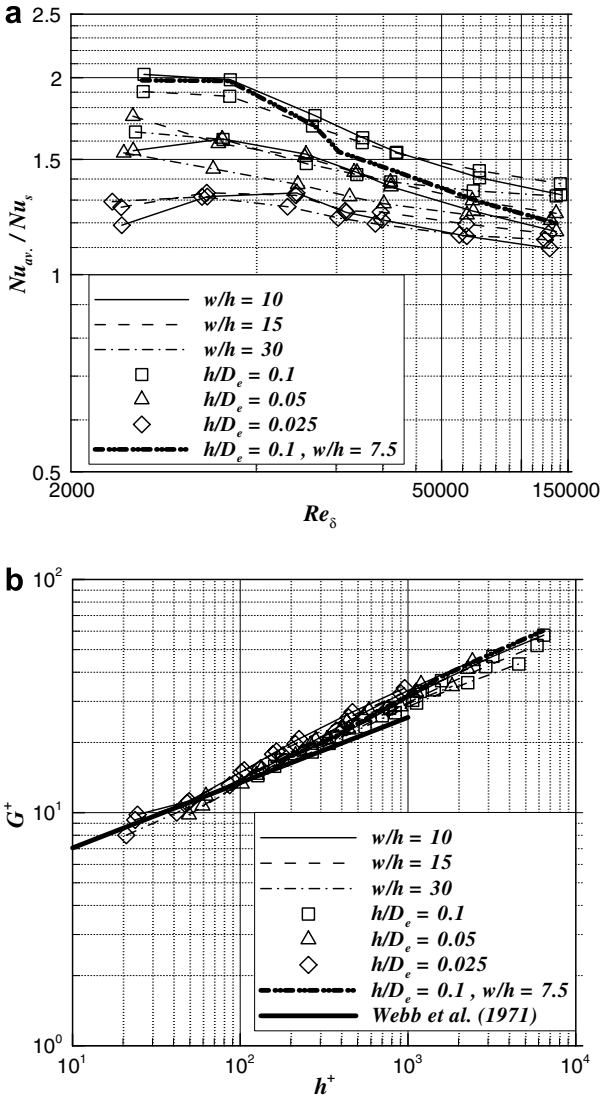

Fig. 12. Heat-transfer characteristics for square ribs: (a) average Nusselt number, (b) heat-transfer roughness function.

shown in Fig. 12b exhibits a logarithmic behavior. All curves are less scattered than for those of different shapes but they do not fall on a single curve. Also, the slope of the present results is seen to be slightly steeper than that of Webb et al.'s correlation (1971).

3.2. Heat transfer over three-dimensional roughness elements

The numerical simulations are extended to three-dimensional flow over uniformly distributed hexahedral blocks. Compared to the two-dimensional cases, there are many more geometric parameters to deal with. For present purposes, however, only two representative block cross-sections are examined as was done in *Part I* for flow resistance: a square section and a rectangular section of spanwise aspect ratio of 2, in in-line and staggered arrangements (see Fig. 13). The transverse block spacing d/D_e and streamwise length of the block b/D_e are held constant at 0.75 and 0.3, respectively. The height is fixed at $h/D_e = 0.1$ as in two-dimensional ribs and thus the streamwise length to height ratio of the block becomes 3. Again, the channel wall and the blocks are assumed to be aluminum and the wall thickness S is taken as $0.0375D_e$ for all cases. The block height and pitch (streamwise spacing) are parameters that are varied. For $w/h = 15$ and 18, a non-uniformly distributed grid of $104 \times 80 \times 61$ cells is used while a grid with $80 \times 80 \times 51$ cells is used for $w/h = 6$, 9 and 12. Among the 80 cells placed in y-direction, 16 are in the substrate region.

Typical cross-plane streamlines and isotherms at $x/D_e = 0.6$ for $w/h = 12$ for blocks in staggered arrangement are shown in Fig. 14. The temperature is seen to be higher under the rectangular block than under the square block. This indicates that the heat transfer is more active through the rectangular block because of a larger block cross-sectional area. Also, due to a strong swirling motion of the rectangular-block case, the air temperature becomes lowest in the middle of the cross-section rather than near the upper wall. This greatly enhances the heat transfer from the surface as shall be seen later.

The space-averaged dimensionless temperature profiles and associated virtual origins for various pitch ratios are shown in Figs. 15 and 16. As in the case of two-dimensional ribs, the temperature profile obeys the similarity law for all cases except for the rectangular blocks in staggered arrangement. This is consistent with the observation that the corresponding velocity profile does not exhibit any log-law region. The location of the virtual origin is seen to decrease with the pitch ratio. The block arrangement does not appear to alter the position of the virtual origin while the size of block cross-section does. Two-dimensional results may be obtained by extending the block in the spanwise direction and are also compared in the figure. Note that this case is different from the two-dimensional cases discussed in the previous section as b/h is 3 (not 1). The location for a two-dimensional case is higher than those for three-dimensional cases because of the larger recirculation region.

The mean Nusselt number for w/h is presented in Fig. 17. The heat transfer is most effective when the rectangular blocks are staggered. This is attributed to the increased mixing due to the strong secondary motion observed in Fig. 14. Although the in-line distribution gives slightly higher value than the staggered arrangement for square blocks, the difference is insignificant beyond the point of maximum Nusselt number. The difference between the two rectangular block arrangements also diminishes as the pitch ratio increases. This may be due to the fact that the spanwise variation of the incoming flow becomes smaller as the pitch ratio increases and the block arrangement becomes less crucial. The heat transfer is seen to be very poor for the two-dimensional case when the pitch ratio is small – because of the cavity-like flow developed in this w/h range – but gradually improves to a value somewhere between the square and rectangular blocks as the pitch

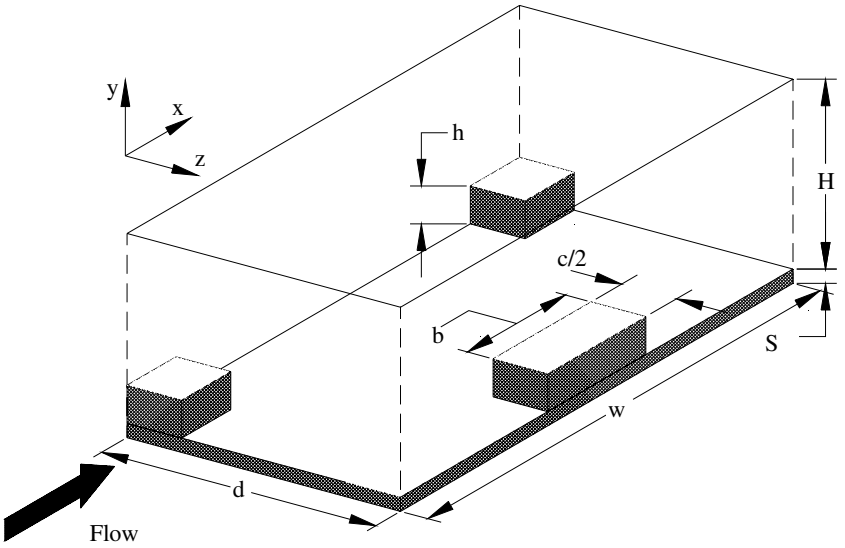

Fig. 13. Schematic of channel with distributed hexahedral blocks in staggered distribution ($h/D_e = 0.1$, $b/D_e = 0.3$, $H/D_e = 0.5$, $d/D_e = 0.75$ are fixed).

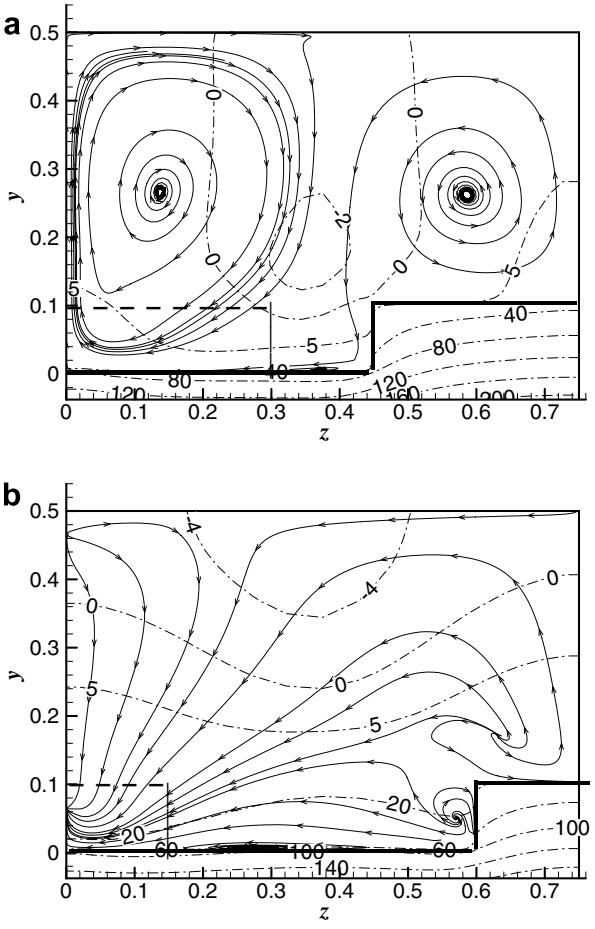

Fig. 14. Streamlines and temperature ($\hat{T}$) field in the streamwise cross-section at $x/D_e = 0.6$ for the $w/h = 12$, $h/D_e = 0.1$ and $Re_{D_e} = 20,000$ for staggered block distribution: (a) $c = 2b$, (b) $c = b$.

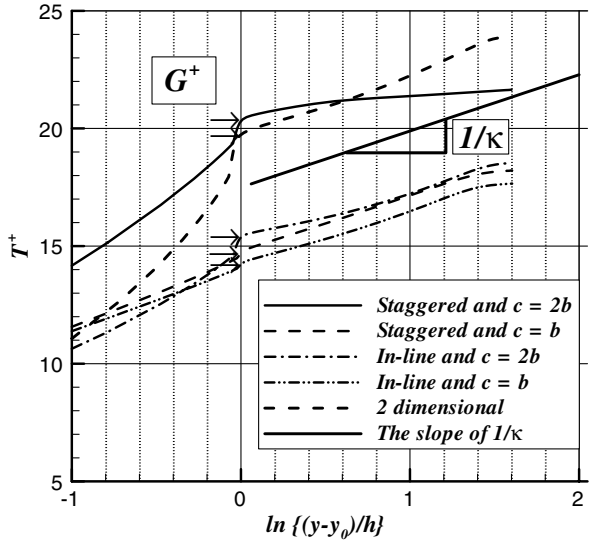

Fig. 15. Space-averaged temperature profiles in wall coordinates for various cases for $w/h = 12$, $h/D_e = 0.1$ and $Re_{D_e} = 20,000$.

ratio increases. This suggests that there may be optimum values for the aspect ratio of the block cross-section and the transverse spacing of the blocks. No attempt has been made to pursue this issue further. The general trend of Nu_{av} is similar to that of resistance discussed in *Part I*. The Nusselt number varies with the resistance factor and becomes largest when the friction factor reaches maximum.

The heat-transfer roughness function is plotted against w/h and h^+ in Fig. 18. In general, G^+ is very small when the pitch ratio is small, increases with pitch ratio up to a maximum, and slowly decreases thereafter. For the staggered case with $c = 2b$, there is no log region in the temperature profile. The variation among the other cases is relatively small but a large difference exists between the three- and two-dimensional cases. The heat-transfer roughness function plotted against h^+ exhibits a similar behavior as in two-dimensional cases: all cases are linear in the log–log scale with the same slope as in the rib cases, a little steeper than that of Webb et al.'s correlation.

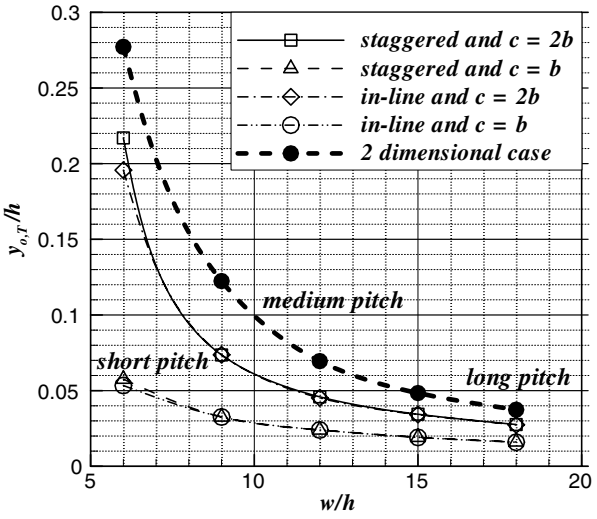

Fig. 16. Location of virtual origin vs. pitch for $h/D_e = 0.1$ at $Re_{D_e} = 20,000$.

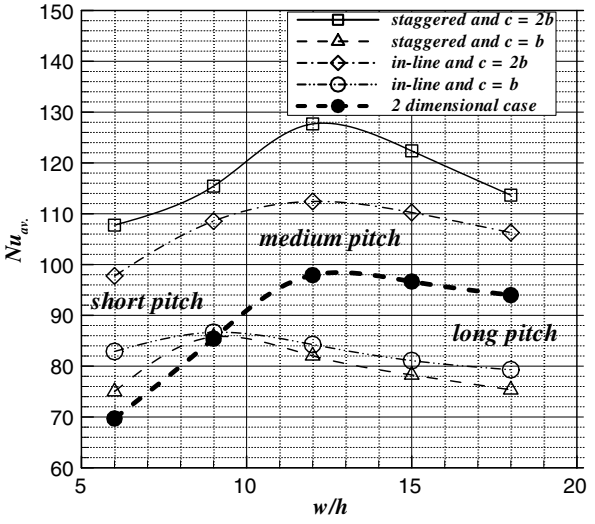

Fig. 17. Average Nusselt number vs. pitch for $h/D_e = 0.1$ at $Re_{D_e} = 20,000$.

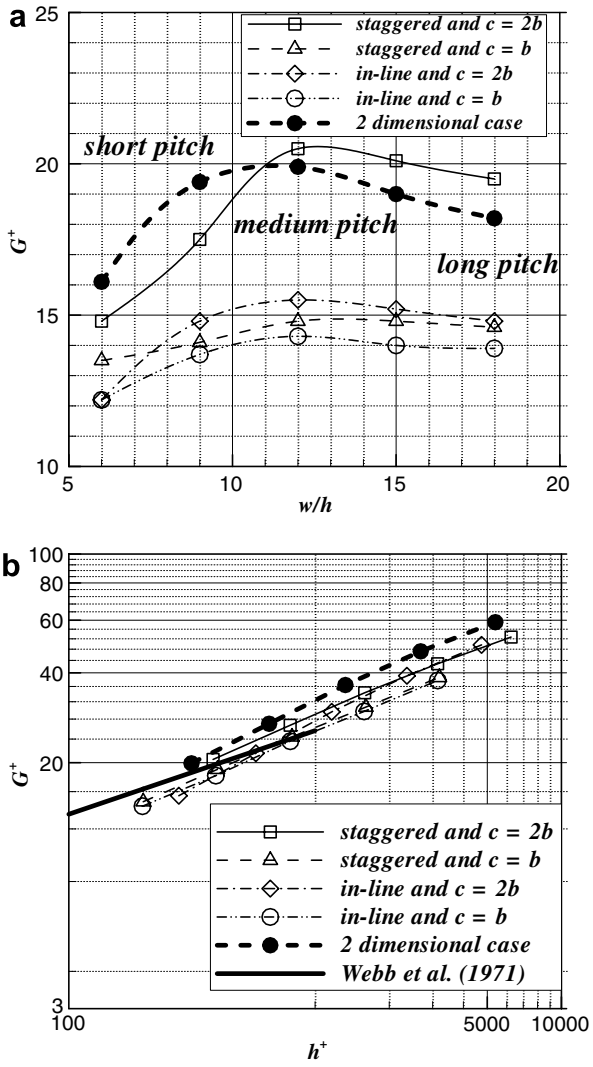

Fig. 18. Heat-transfer roughness function for $h/D_e = 0.1$: (a) vs. pitch at $Re_{D_e} = 20,000$, (b) vs. h^+ for $w/h = 12$.

4. Conclusions

Following the application of the numerical model, based on the Reynolds-averaged Navier–Stokes equations coupled with the k–ω turbulence model, to study the resistance properties of the flow over surfaces with two-dimensional ribs or three-dimensional blocks, the present paper examines the heat-transfer characteristics. It is shown that when solutions are space-averaged over appropriate areas, they provide engineering information about the Nusselt number and its dependence on geometric and flow parameters. In addition, the numerical model provides details of the temperature profile, such as the heat-transfer roughness function, and the virtual origin, that have been the purview of experimental correlations, as well as detailed information about the heat transfer around the roughness elements. Among major findings of this study are:

1. The space-averaged temperature profile varies logarithmically in a region beyond the roughness layer when the distance is measured from a virtual origin and the corresponding velocity profile has a logarithmic region. The slope remains close to κ^{-1} but the virtual origin of the temperature profile is much closer to the bottom of the roughness than that of the velocity profile.
2. The log of the heat-transfer roughness function G^+ varies linearly with the log of the roughness Reynolds number h^+. The slope of the correlation seems to be the same for both two-dimensional ribs and three-dimensional blocks, but it is somewhat steeper than that of the experimental correlation in Webb et al.
3. The geometry for maximum heat transfer, i.e., highest average Nusselt number, corresponds to that of maximum resistance coefficient for both two-dimensional ribs and three-dimensional blocks.

The numerical model developed here appears to be capable of resolving details of the flow and heat-transfer

from a wall with geometrically simple roughness. These details are difficult to measure and quantify by experiments. The model may be used to further understanding of the interaction between the spatially non-uniform flow in the roughness layer and the outer flow that feels only an averaged effect of a rough wall.

Acknowledgements

This work was supported by KISTEP under Grant 2-578 through the National Research Lab. Program and, in part, by KOSEF through Combustion Engineering Research Center. The authors thank IIHR – Hydroscience & Engineering, The University of Iowa, for support of this collaborative research. Referees' useful comments that helped ameliorate the paper are also greatly appreciated.

References

Abe, K., Kondoh, T., Nagano, Y., 1995. A new turbulence model for predicting fluid flow and heat transfer in separating and reattaching flows – II. Thermal field calculations. Int. J. Heat Mass Transfer 38, 1467–1481.

Acharya, S., Dutta, S., Myrum, T.A., Baker, R.S., 1993. Periodically developed flow and heat transfer in a ribbed duct. Int. J. Heat Mass Transfer 36, 2069–2082.

Bejan, A., 2004. Convection Heat Transfer. third ed.. John Wiley & Sons, New Jersey, p. 393.

Dipprey, D.F., Sabersky, R.H., 1963. Heat and momentum transfer in smooth and rough tubes at various Prandtl number. Int. J. Heat Mass Transfer 6, 329–353.

Han, J.C., 1988. Heat transfer and friction characteristics in rectangular channels with rib turbulators. ASME J. Heat Transfer 110, 321–328.

Han, J.C., Glicksman, L.R., Rohsenow, W.M., 1978. An investigation of heat transfer and friction for rib-roughened surfaces. Int. J. Heat Mass Transfer 21, 1143–1156.

Hayase, T.J., Humphrey, A.C., Grief, R., 1992. A consistently formulated QUICK scheme for fast and stable convergence using finite-volume iterative calculation procedure. J. Comput. Phys. 98, 108–118.

Iaccarino, G., Ooi, A., Durbin, P.A., Behnia, M., 2002. Conjugate heat transfer predictions in two-dimensional ribbed passages. Int. J. Heat Fluid Flow 23, 340–345.

Kasagi, N., Kuroda, A., Hirata, M., 1989. Numerical investigation of near-wall turbulent heat transfer taking into account the unsteady heat conduction in the solid wall. J. Heat Transfer 111, 385–392.

Kays, W.M., 1994. Turbulent Prandtl number – Where are we? J. Heat Transfer 116, 284–295.

Kays, W.M., Crawford, M.E., 1993. Convective Heat and Mass Transfer. third ed.. McGraw-Hill, pp. 259–274.

Lee, B.K., Cho, N.H., Choi, Y.D., 1988. Analysis of periodically fully developed turbulent flow and heat transfer by k–ε equation model in artificially roughened annulus. Int. J. Heat Mass Transfer 31, 1797–1806.

Liou, T.M., Hwang, J.J., 1993. Effect of ridge shapes on turbulent heat transfer and friction in a rectangular channel. Int. J. Heat Mass Transfer 36, 931–940.

Liou, T.M., Hwang, J.J., Chen, S.H., 1993. Simulation and measurement of enhanced turbulent heat transfer in a channel with periodic ribs on one principal wall. Int. J. Heat Mass Transfer 36, 507–517.

Manceau, R., Parneix, S., Laurence, D., 2000. Turbulent heat transfer predictions using the model on unstructured meshes. Int. J. Heat Fluid Flow 21, 320–328.

Nagano, Y., Hattori, H., Houra, T., 2004. DNS of velocity and thermal fields in turbulent channel flow with transverse-rib roughness. Int. J. Heat Fluid Flow 25, 393–403.

Okamoto, S., Seo, S., Nakaso, K., Kawai, I., 1993. Turbulent shear flow and heat transfer over the repeated two-dimensional square ribs on ground plane. Trans. ASME J. Fluids Eng. 115, 631–637.

Rau, G., Cakan, M., Moeller, D., Arts, T., 1998. The effect of periodic ribs on the local aerodynamic and heat transfer performance of a straight cooling channel. ASME J. Turbomach. 120, 368–375.

Ryu, D. N, Choi, D.H. Patel, V.C., in press. Analysis of turbulent flow in channels roughened by two-dimensional ribs and three-dimensional blocks. Part I: Resistance, Int. J. Heat Fluid Flow. doi:10.1016/j.ijheatfluidflow.2006.11.006.

Seki, Y., Kawamoto, N., Kawamura, H., 2003. Proposal of turbulent heat flux model with consideration of linearity and its application to turbulent channel flow with various thermal boundary conditions. In: Hanjalic, K., Nagano, Y., Tummers, M.J. (Eds.), Turbulence, Heat and Mass Transfer, vol. 4, pp. 569–576.

Sparrow, E.M., Tao, W.Q., 1983. Enhanced heat transfer in a flat rectangular duct with streamwise-periodic disturbances at one principal wall. Trans. ASME J. Heat Trans. 105, 851–861.

Tafti, D.K., 2005. Evaluating the role of subgrid stress modeling in a ribbed duct for the internal cooling of turbine blades. Int. J. Heat Fluid Flow 26, 92–104.

Vogel, J.C., Eaton, J.K., 1985. Combined heat transfer and fluid dynamic measurements downstream of a backward-facing step. Trans. ASME J. Heat Transfer 107, 922–929.

Webb, R.L., Eckert, E.R.G., Goldstein, R.J., 1971. Heat transfer and friction in tubes with repeated-rib roughness. Int. J. Heat Mass Transfer 14, 601–617.

Wilcox, D.C., 1998. Turbulence Modeling for CFD. second ed.. DCW Industries.